# Breaking the limitation of sodium-ion storage for nanostructured carbon anode by engineering desolvation barrier with neat electrolytes

Yichao Zhen [a,1], Rongjian Sa [b,1], Kaiqiang Zhou [a,c], Lingyi Ding [a], Yang Chen [a], Sanjay Mathur [d,**], Zhensheng Hong [a,d,*]

[a] *Fujian Provincial Key Laboratory of Quantum Manipulation and New Energy Materials, College of Physics and Energy, Fujian Normal University, Fuzhou, Fujian, 350117, China*
[b] *Institute of Oceanography, Minjiang University, Fuzhou, Fujian, 350108, PR China*
[c] *Fujian Provincial Collaborative Innovation Center for Advanced High-Field Superconducting Materials and Engineering, Fuzhou, 350117, China*
[d] *Institute of Inorganic Chemistry, University of Cologne, Greinstr. 6, 50939, Cologne, Germany*

ABSTRACT

In the past, most of the studies monotonously focused on developing electrode materials for sodium ion batteries (SIBs), while the compatibility effects and mechanism of electrolytes with material microstructures on the sodiation behavior are barely involved. Here, we demonstrate the sodium-ion storage behavior of carbon anode in neat ether electrolytes with outstanding ion diffusion kinetics at electrode surface that breaks its innate limitation. Porous nanocarbon with small interlayer spacing but very high surface area exhibits a record high ICE over 91.1% and exceptional rate capability for Na-ion storage in ether-based electrolytes. This is due to the remarkably reduced $Na^+$ desolvation barrier in ether electrolytes ($\sim$94.6 meV) that is less than one-third of that in ester electrolytes ($\sim$307.8 meV). The strong interaction of Na-ions with ester electrolytes and their decomposition on electrode surface can be suppressed by adopting ether solvents owing to lower Gibbs free energies of solvation and $Na^+$ desolvation energy as revealed by DFT calculations. For electrode materials working with ether electrolytes, a large surface area is critical for better electrochemical performance. This study provides a reliable regulation parameter for tailoring electrolytes with materials that offers promising potential for nanostructured materials toward high-rate rechargeable devices.

## 1. Introduction

The large-scale application of lithium-ion batteries (LIBs) is confronted with the problems of limited lithium resources and its uneven geographical distribution [1,2]. In this context, the room temperature sodium-ion batteries (SIBs) are considered as a promising alternative to LIBs, especially in large-scale energy storage system due to abundance of sodium on the earth as well as its environmental friendly nature [3,4]. Therefore, SIBs have received widespread attention [5–9] and a variety of new materials have been developed as potential anodes for SIBs containing non-graphitic carbon-based materials [10–15], alloy reaction material (P, Sn, etc) [16–18] and conversion-type reaction material [19–22], as well as Ti-based oxides [23–26]. Among various possible

anode materials, non-graphitic carbon anode is considered as the best choice in view of easy availability and easy production in large scale.

As one of the earliest negative electrodes of SIBs, non-graphitic carbon including hard carbon or disordered carbon displayed high sodium intercalation activity due to larger interlayer spacing of disordered carbon (0.37–0.39 nm) when compared to crystalline graphite ($\sim$0.34 nm) to become a leading candidate material for SIB anode [14,27–32]. Only Na-solvent cointercalation can happen due to the Na instability in graphite structure [33–36]. Thus, many efforts have been devoted to prepare hard carbon or amorphous carbon materials with larger interlayer spacing for easy Na-ion insertion with enhanced capacity and rate capability [10,37–40]. It should be noted that the yield of large-spacing carbon is generally achieved by heteroatom-doping (O, N, P, S, etc.) with

---

elements consisting of larger atomic radius that augments the storage capacity as well. However, a large irreversible capacity is usually intrinsic to these nanocarbon materials [41,42]. Previous study proposed that Na ions would be trapped at defect sites on graphite basal planes because of their strong adsorption energy [43–45], resulting in large migration or diffusion barriers for Na ions. Accordingly, in the most common ester electrolytes, like propylene carbonate (PC), ethylene carbonate (EC) and diethyl carbonate (DEC), nanostructured carbons usually exhibit a low initial Coulombic efficiency (ICE) [46–49]. This is due to the generation of a solid electrolyte interphase (SEI) film that leads to the irreversible consumption of $Na^+$ at the electrode surface [50]. Recently, several studies reported that carbon electrodes displayed enhanced ICE and superior rate performance in an ether-based electrolyte [51–55] ascribable to the production of a thinner SEI on electrode surface accompanying with significantly reduced charge-transfer resistance. However, the performance still needs to improve, and essential cooperation mechanism of ether electrolyte with electrode material are far from elucidation especially from the view point of chemical properties of solvents.

In this work, we overcame two limitations of sodium-ion storage for nanocarbon anode by adopting compatible and neat ether electrolytes namely to reduce the electrolyte decomposition and to demonstrate a highly reversible and fast sodiation behavior in small interlayer spacing (<0.36 nm). Our results show that porous carbon material with ultra-large surface area exhibits a record high ICE over 91.1%, exceptional intercalation/extraction kinetics and long cyclic life for Na-ion storage. It's revealed that $Na^+$ desolvation and diffusion barrier at the electrode surface and interface play a predominant role on the sodium-ion storage performance. The $Na^+$ desolvation barrier in ether electrolytes is less than one third of that in ester electrolytes, leading to enhanced kinetics and remarkably improved ICE. This result is verified by DFT calculations that the Na-ion desolvation energy in ether-based solvent is much lower than that in ester-based solvent. More importantly, the strong adsorption and decomposition of electrolytes on graphene planes is remarkably reduced in ether solvents due to the decreased Gibbs free energies of adsorption.

## 2. Results and discussion

The porous nanocarbon (PNC) with large surface area but small interlayer spacing was synthesized by a molten salts method following a previous study [10]. As shown in Fig. S1a, the porous nanocarbon with sulfur doping and nanosheets morphology exhibited broad diffractions peaks, indicating an amorphous structure of as-prepared carbon material with an estimated d-spacing of 3.54 Å for PNC deduced from the 2θ values in the XRD pattern. A mesoporous structure with large pore volume of 1.465 $cm^3$ $g^{-1}$ with ultra-large surface area up to 1023.6 $m^2$ $g^{-1}$ was observed (Fig. S1b) that was confirmed by the SEM image (Fig. S1c) revealing a nanosheet-like morphology and a porous nature. HRTEM images in Fig. S1d as well as corresponding SAED pattern further verified the poorly crystalline nature of such material with an approximate d-spacing determined to be around 0.36nm.

The galvanostatic discharge and charge tests investigated in different kinds of ester and ether electrolytes showed (Fig. 1) very large first discharge capacities of 1694.2 and 1458.1 mA h $g^{-1}$ at 0.1 A $g^{-1}$ in PC and EC/DMC electrolytes, but the charge capacities were found to only 594 and 636.1 mA h $g^{-1}$. On the contrary, the first discharge capacities of 866.5 and 630.5 mA h $g^{-1}$ were obtained in DME and DEGDME electrolytes, with corresponding charge capacity values of 632.3 and 562.2 mA h $g^{-1}$, respectively. It's remarkable that the ICE in ether electrolytes is much higher than in ester-based solvents. The ICE greatly increased from 35.1% (PC) and 43.6% (EC/DMC) in ester to 72.9% (DME) and 89.2% (DEGDME) in ether electrolytes. Fig. 1e describes the rate capability of PNC in DME, DEGDME, EC/DMC and PC electrolytes at various current densities. The electrode in ester electrolytes (EC/DMC, PC) displayed fast capacity fading with an increasing rate with less than 20 mAh $g^{-1}$ remaining above rates of 5 A $g^{-1}$. By contrast, PNC in ether electrolytes exhibits remarkably excellent rate capability in ether electrolytes and even at a very high rate of 20 A $g^{-1}$, large capacities of 331.3 mA h $g^{-1}$ in DME and 296 mA h $g^{-1}$ in DEGDME were retained, demonstrating the fast kinetics of sodium-ion storage. Besides, PNC electrode in DME electrolyte showed much better cycling performance than in PC electrolyte, as presented in Fig. 1f. A significant capacity retention (486 mA h $g^{-1}$) was observed in DME (only 115 mA h $g^{-1}$ in PC) after one thousand cycles at 1 A $g^{-1}$. The PNC electrode displays a high Coulombic Efficiency around 100% after 3 cycles in ether
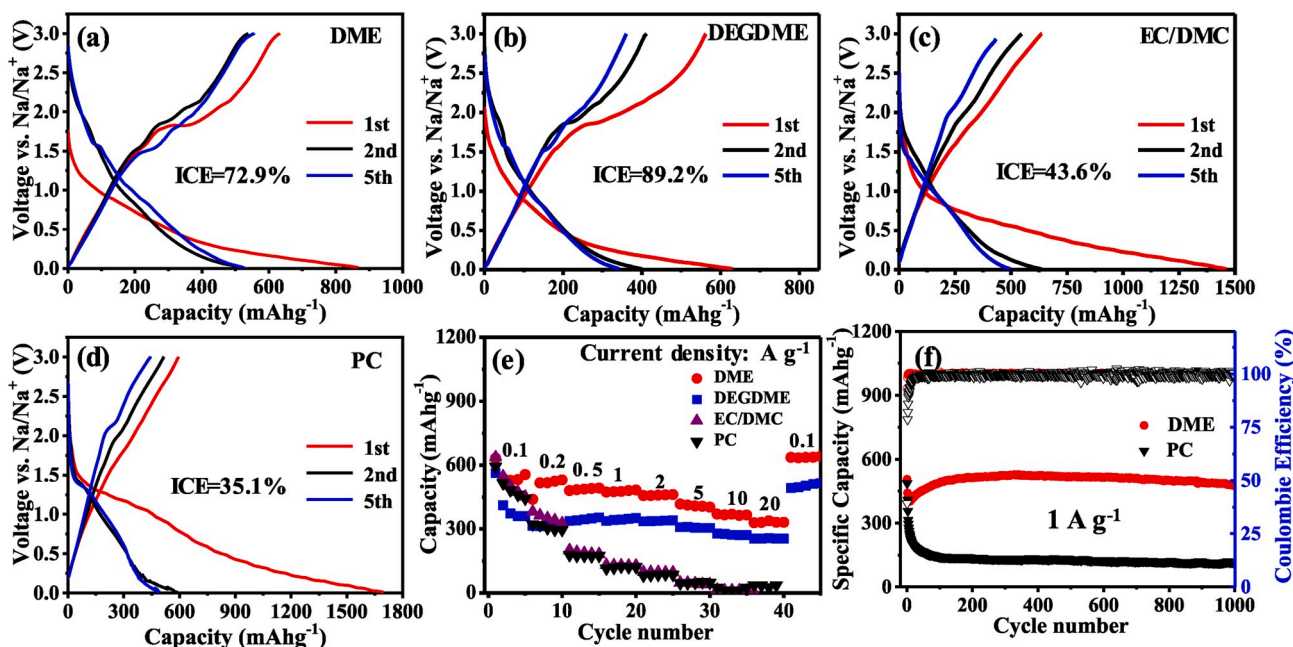


**Fig. 1.** Discharge and charge profiles for the 1st, 2nd and 5th cycles of PNC electrodes (PVDF) in (a) DME, (b)DEGDME, (c) EC/DMC and (d) PC electrolytes at a rate of 0.1 A $g^{-1}$, (e) rate performance of PNC in different electrolytes at different rate, long cycling stability of PNC electrodes at a constant current density of 1 A $g^{-1}$.

electrolytes which is much better than in ester electrolytes.

Transport behavior and kinetic performance of Na$^+$ across the PNC electrode in DME and EC/DMC electrolytes were investigated by CV, as displayed in Fig. 2a–b. CV curves at initial cycle and the following cycles are shown Fig. S2a and Figs. S2b and a large irreversible reaction in EC/DMC electrolytes for PNC electrodes is observed at the first cycle while it doesn't occur in DME electrolytes. Moreover, the redox peaks in ether electrolytes is much reversible and remarkable compare to ester electrolytes, suggesting the significantly enhanced reaction kinetics. Besides, a small anodic peak at the first cycle in both two cases is observed and will gradually disappear, which may be due to the irreversible absorption of anions to sulfur atoms. The peaks denoted as A, B, C and D in voltammetry curves were selected to investigate the charge storage mechanisms. A, B and D peaks are contributed to the redox reaction of sodium-ion with sulfur heteroatoms, and peak C belongs to the intercalation of sodium-ion into graphene layer [10,37]. It is evident that the electrode in DME electrolyte displayed significantly superior kinetics with nearly no polarization between 0.1 mV s$^{-1}$ and 20 mV s$^{-1}$, however, the electrode suffered from low activity with no apparent redox peaks and large polarization. Charge storage process was analyzed according to $i = av^b$. For A and B peaks, the b values are 0.797 and 0.789 for the DME, suggesting that diffusion-controlled and pseudo-capacitive controlled process are concomitant. Thus, ether electrolyte may boost the surface capacitive storage for PNC electrode due to the outstanding kinetics. While in the EC/DMC, there are no A and B peaks, indicating insufficient electrochemical activity. For C and D peaks, the b values obtained from DME and EC/DMC are all close to 1 indicating a pseudo-capacitive controlled Na$^+$ storage behavior. The diffusion-controlled and capacitive controlled capacity can be quantified proposed by B. Dunn according to the formula: $i(V) = k_1 v + k_2 v^{1/2}$ [56,57]. As shown in Fig. S2c and Fig. S2d, the capacitive controlled capacity is relative constant in the range of 79-88% from 0.1 to 20 mV s$^{-1}$.

We used galvanostatic intermittent titration technique (GITT) to investigate the diffusion coefficient of Na-ion in PNC electrode. As depicted in Fig. 2c–f, PNC electrode at different electrolytes has similar

diffusivity coefficient variation. Therefore, the significantly improved Na-ion storage performance including ICE and superior kinetics is not due to enhanced diffusion ability in bulk. It should be noted that same structure change after sodiation in different electrolytes are also revealed from Raman (Figs. S3a and b) and TEM images (Figs. S3c and d). A bit increases in layer spacing after sodiation in both two cases could be due to the Na-ion interaction into the graphene layer. The presence of Na-solvent cointercalation hardly occur because the structure and layer spacing would be remarkably changed in this case that happened in graphite anode [34]. Moreover, the same structure change in different electrolytes also indicate the crucial influence on the Na-ion storage performance is not determined from the change of bulk structure or possible solvent interaction with bulk structure. Thus, it's suggested that the key effect on the Na-ion storage should be governed by the ion transport on the material surface instead of the bulk structure.

In order to analyze a possible interference and complexity of SEI film in anode material and to understand the desolvation behavior, we firstly tested the cathode material, Na$_2$V$_3$(PO$_4$)$_3$ (NVP) as a perfect intercalation host in DME and EC/DMC electrolytes. Such cathode also displayed improved Na-ion storage performance as demonstrated in our previous study [52]. The AC impedance spectra for NVP cathode in DME and EC/DMC electrolytes at various temperatures showed after five discharge-charge cycles (Fig. 3a–b). Nyquist plots with only one semi-circle in the wide frequency of 0.1–10$^6$ Hz. In the absence of an interphase, the only semicircle should be attributed to the so-called charge-transfer ($R_{ct}$) resistance. However, the desolvation barrier could be the dominant reason for this resistance based on the same host structure, but showing different properties in ether and ester electrolytes [58,59]. The $R_{ct}$ in EC/DMC electrolyte impetuously increases (more than 2500 Ω) with the decline of temperature to 0 °C, while it increases a little in DME electrolyte. By fitting the semicircle to an equivalent circuit through software ZSimpwin, we could calculate that the resistance belong to "charge-transfer" process ($R_{ct}$) and the derived activation energy ($E_{ct}$) through the temperature dependence of $1/R_{ct}$. Fig. 3c presents the Arrhenius behavior for this thermally activated process of Na$^+$ desolvation on NVP surface and the resulting activation energies in
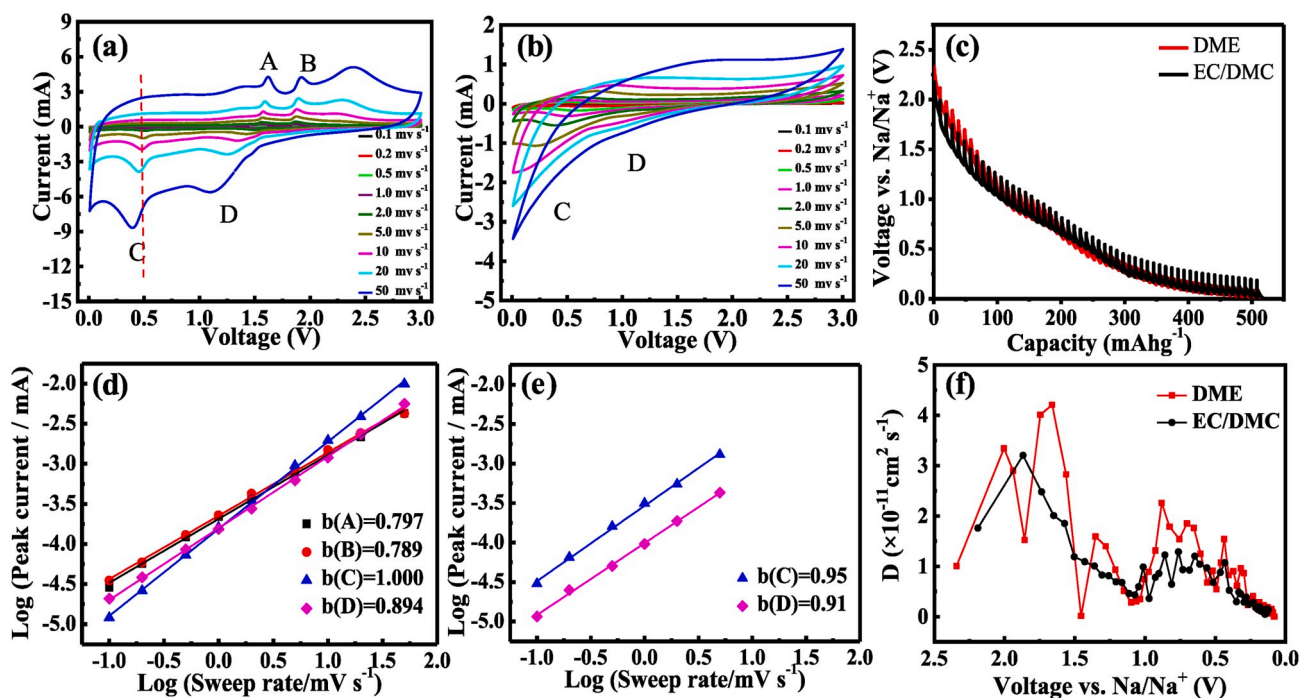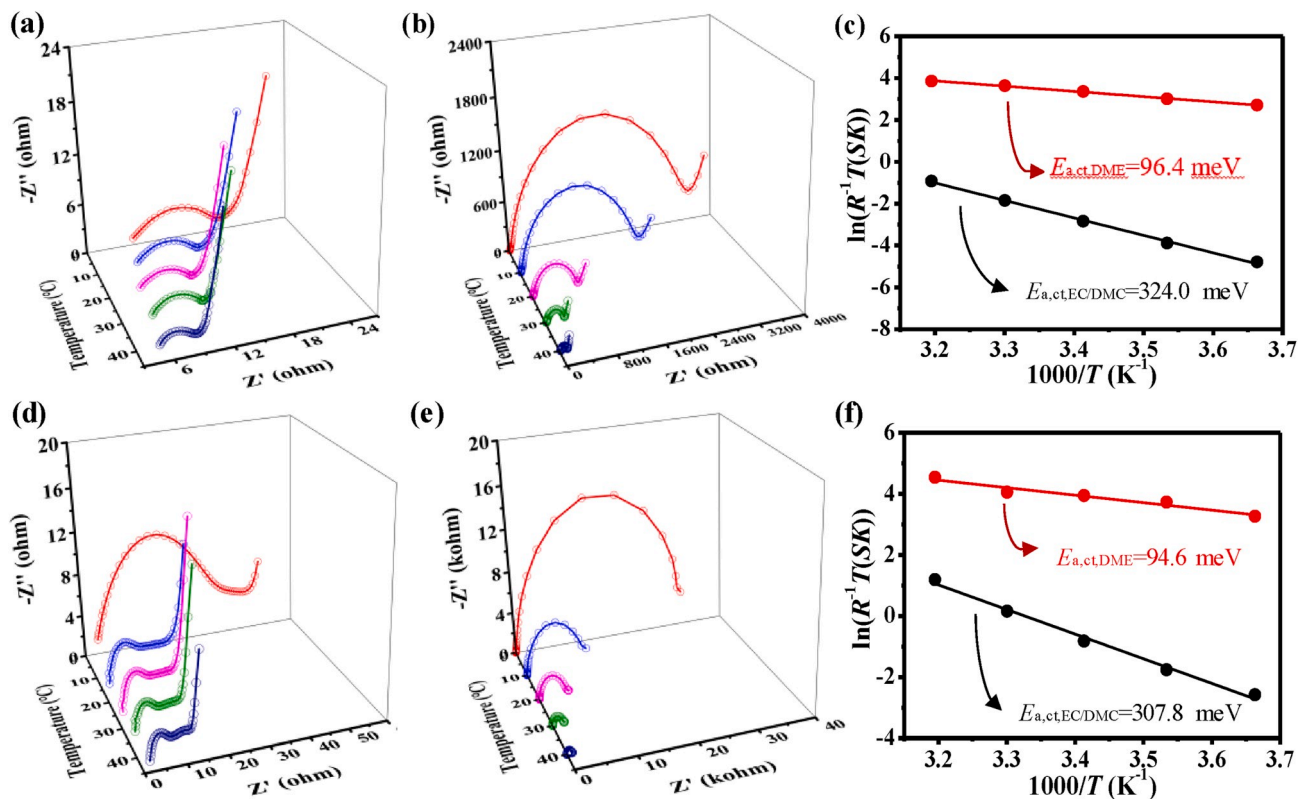


**Fig. 2.** CV curves sweep rate of 0.1-50 mV s$^{-1}$ for PNC electrodes in (a) DME and (b) EC/DMC. The translation of logarithmic format for PNC electrodes in (d) DME and (e) EC/DMC. (c) GITT potential profiles of the two electrodes for sodiation process during the second cycle and (f) Na-ion diffusion coefficients calculated from the GITT potential profiles.

**Fig. 3.** Temperature-dependent Nyquist plots of the NVP cathode for (a) DME-based electrolyte and (b) the EC/DMC-based electrolyte. (c) Arrhenius plot of activation energies $E_{a,ct}$ for the NVP cathode in two electrolytes. Temperature-dependent Nyquist plots of PNC anode in (d) DME-based electrolyte and (e) the EC/DMC-based electrolyte. (f) Arrhenius plot of activation energies $E_{a,ct}$ for PNC anode in two electrolytes.

different electrolytes. The Arrhenius equation is used to determine the activation energies [60]: $\sigma T = A\exp(-E_a/k_B T)$. Here, A is the pre-exponential factor, $E_a$ is the apparent activation energy for ion transport, $k_B$ is the Boltzmann constant, $\sigma$ is the ionic conductivity, and T is the absolute temperature. In EC/DMC electrolyte the activation energy across the interface ($E_{a,ct}$, EC/DMC) is up to ~324.0 meV, which is 3.4 times higher than that observed in DME electrolyte (96.4 meV).

After the activation energies were determined in different electrolytes, the PNC anodes were also investigated by the same route. Fig. 3d–e show Nyquist plots of PNC anode after 5 cycles discharged to 0.5 V in DME and EC/DMC electrolytes at various temperatures. Two semicircles were observed in the impedance spectra in DME electrolyte that are usually ascribed to interphase resistance $R_{sf}$ at high frequency and $R_{ct}$ at low frequency. The resistance in EC/DMC electrolyte increased sharply and was found to be much larger than that in DME electrolyte. As shown in Fig. 3f, the temperature dependencies (Arrhenius plots) of $1/R_{ct}$ in DME and EC/DMC electrolytes revealed that the $E_{a,ct}$ is ~94.6 meV in DME electrolyte and is ~307.8 meV in EC/DMC electrolyte. The values were comparable with those obtained from NVP cathode, which suggests that the Na-ion desolvation barrier could be responsible for the main resistance. The Na$^+$ activation energy for diffusion in the SEI layer $E_{a,SEI}$ for the two cases are shown in Fig. S4. In EC/DMC electrolyte, the activation energy across the interface ($E_{a,SEI}$, EC/DMC) is up to ~282.0 meV, which is 4 times higher than that in DME electrolyte (70.7 meV). This suggests the formation of a thick SEI layer, and is different from the case of titanium dioxide, which possessed similar $E_{a,SEI}$ in ether and ester electrolytes [53].

In order to reveal the intrinsic chemical properties of different electrolytes, DFT calculations were adopted to explore the Na-ion desolvation energies, as show in Fig. 4a and Fig. S5. It was found that both Na-DME and Na-DEGDME complex exhibit much lower de-solvation energies compared with traditional Na-ester solvent complex,

suggesting the easier de-solvation process in former cases. Nevertheless, the explanation of significantly enhanced performance and a suppressed decomposition of electrolytes toward dramatically improved ICE in ether electrolytes required further elaboration such as the Gibbs free energies of adsorption of Na$^+$-solvent on the electrode surface. As shown in Fig. 4b, Fig. S6 and Table S1, our theoretical data showed that the adsorption of Na$^+$ cation and solvent on graphene plane is an energetically favorable process for the negative $\Delta G$ values. The adsorption of Na$^+$-ester on the surface of electrode material is much stronger than that of Na$^+$-ether due to their large Gibbs free energies of adsorption, in absolute values. Such decreased adsorption energies will further boost the Na$^+$ transport on the electrode surface and is apparently the main reason for the electrolyte decomposition observed in ester electrolytes when compared to ether electrolytes. The EDX analysis (Table S2) of PNC samples showed higher contents of adsorbed Na, F elements in ester electrolytes determined after dipping the samples into the electrolytes. The comparative study of carbon materials with different surface areas prepared from the same route were also evaluated for the sake of proving this suggestion. As shown in Fig. S7, Fig. S8 and Table S3, PNC-p and NC-p display lower capacity in ether electrolytes than that in ester electrolytes, and even lower ICE for NC-p. This interesting finding demonstrates that the larger the surface area is, the better is the electrochemical performance achieved for electrode material in ether electrolytes. This result agrees well with above suggestion about the surface-determined effect based on experimental characterization and theoretical calculation. Na ions would be easily trapped in nanocarbon materials due to intensive adsorption activity [43–35], and this problem will be accentuated in ester electrolytes with large Na$^+$-ester Gibbs free energies of adsorption on the surface, leading to poor ion transport and large reversible capacity. On the contrary, the large surface area or porous structure for electrode material is necessary and favor for Na-ion storage in ether electrolytes because it's too neat nature to capture due
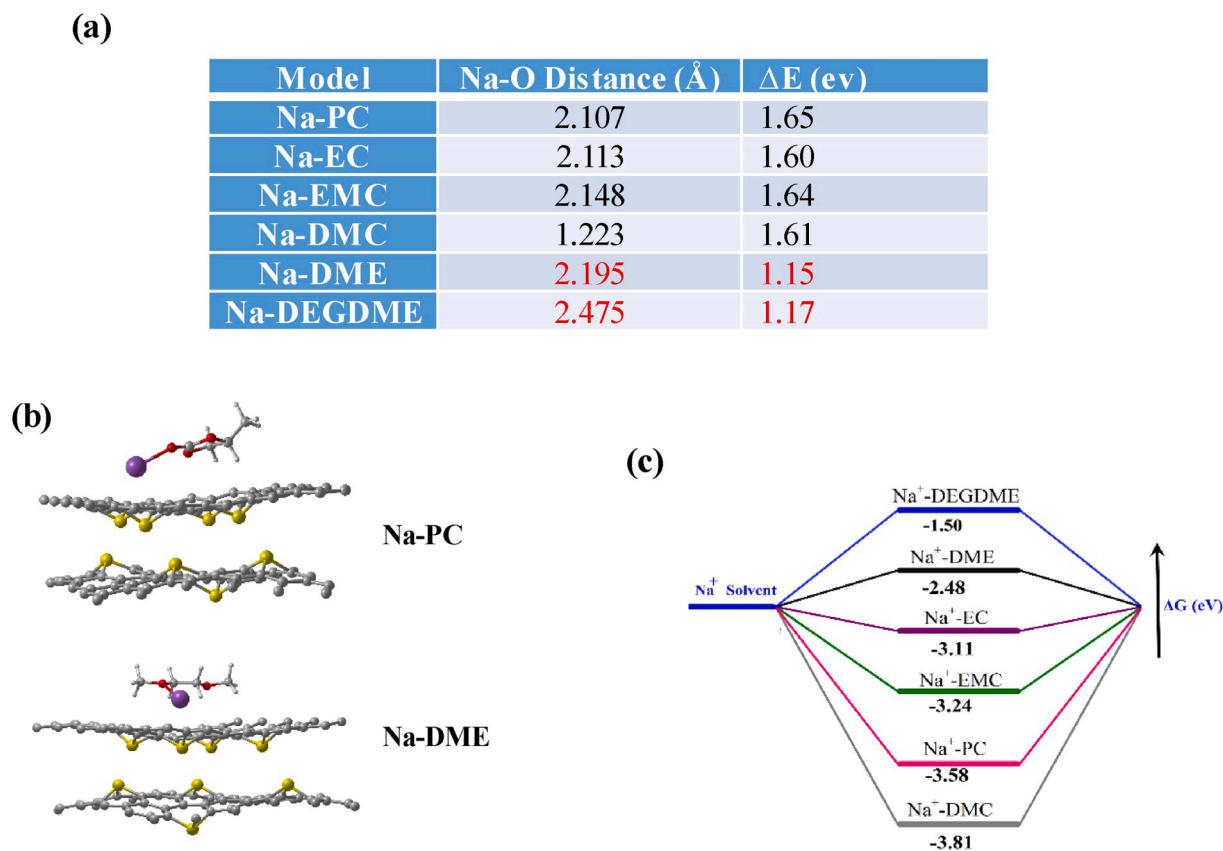
**(a)**

| Model | Na-O Distance (Å) | ΔE (ev) |
|---|---|---|
| Na-PC | 2.107 | 1.65 |
| Na-EC | 2.113 | 1.60 |
| Na-EMC | 2.148 | 1.64 |
| Na-DMC | 1.223 | 1.61 |
| Na-DME | 2.195 | 1.15 |
| Na-DEGDME | 2.475 | 1.17 |

**(b)**



Na-PC

Na-DME

**(c)**



Fig. 4. (a) Optimized structure data and energies data for Na-solvent complex. (b) Optimized adsorption configurations of $Na^+$-solvent on the surface of sulfur doped graphene and (c) the corresponding absorbed Gibbs free energies on the material surface.

to the too low $Na^+$-ether adsorption ability. In addition, the remarkably lower dynamic viscosity of ether electrolytes (0.71 mPa s for DME) than ester electrolytes (2.12 mPa s for EC/DMC) measured by rotary viscometer also help us understand the neat nature of ether electrolytes for faster mass transport. As a result, the larger surface area of electrode material is, the better performance it delivers in neat ether electrolytes, but has opposite result in sluggish ester electrolytes. This result further verified the absorbed Gibbs free energies of $Na^+$-solvent is a reliable parameter to evaluate the complicated sodiation dynamics and properties.

In order to further prove the concept of surface effects playing a dominant role on Na-ion storage performance, another binder CMC with carboxylic acid functional groups was used and investigated for PNC anode. The discharge/charge profiles of PNC with CMC binder in DME and DEGDME electrolytes are presented in Fig. 5a and b. The discharge capacities obtained in DME and DEGDME electrolytes were 572.1 mA h $g^{-1}$ and 593.9 mA h $g^{-1}$ after the first cycle, and the charge capacities were 521.4 mA h $g^{-1}$ and 531.0 mA h $g^{-1}$, respectively. Therefore, exceptional high ICE up to 91.1% in DME electrolyte and 89.4% in DEGDME electrolyte were obtained with further improved performance compared to PVDF binder. The ICE of typical commercial mesoporous carbon (CMK-3) and active carbon (AC) anodes with large surface area has also been significantly improved by combining ether-based electrolytes with CMC binder, as shown in Fig. S9. The ICE for CMK-3 and AC increased from 20.3% (EC/DMC) to 70.3% (DME) and from 18.8% (EC/DMC) to 84.0% (DME), respectively. Fig. 5c describes the rate capability of PNC with CMC binder in DME, DEGDME electrolytes at various current densities. It shows that PNC in DME electrolyte displayed high capacity from 521.4 to 356.6 mA h $g^{-1}$ from 0.1 to 20 A $g^{-1}$. As shown in Fig. 5d, a capacity of ~622.2 mA h $g^{-1}$ is remained after 100 cycles at 0.1 A $g^{-1}$. Fig. 5e shows the long cycling life of the PNC at a high current density of 5 A $g^{-1}$ with ~290 mA h $g^{-1}$ retained even after 3600 cycles,

demonstrating excellent cycling stability of such electrode in DME electrolyte. Because of the porous structure of the electrode material, the electrolyte will gradually enter the material as the electrochemical reaction proceeds, resulting to gradually increased capacity in the first 20 cycles [61]. The comparison of electrochemical performance show in Table S4 highlight our breakthrough of Na-ion storage performance about carbon electrodes. Further, full cells were assembled with PNC anode and $Na_3V_2(PO_4)_3F$ (NVPF) as a cathode in DEGDME electrolyte to investigate the practicability, as shown in Fig. S10b. The cell displayed a large capacity of 388.1 mA h $g^{-1}$ at 0.2 A $g^{-1}$, and delivered 335.6 mA h $g^{-1}$ at 2 A $g^{-1}$ (The discharge capacity computed for the full cell is based on the anode), demonstrating excellent rate performance. Moreover, it also exhibited good cycling stability under a constant current of 0.5 A $g^{-1}$ (Fig. S10c).

Although polymeric binders with carboxylic acid functional groups have been proposed to improve Li or Na ion interaction [52,62,63], the intrinsic surface effect and mechanism needs to be illustrated from the side of Na-ion desolvation process at the electrode surface. Fig. 5f and g show selected Nyquist plots at selected temperatures and the corresponding Arrhenius plots of the $1/R_{ct}$ for PNC anode with CMC binder in DME electrolyte. It is noteworthy that only one semicircle can be observed for PNC with $E_{a,ct}$ calculated to be ~79.5 meV. This value is smaller than that of PVDF binder, suggesting the reduced Na-ion desolvation barrier. Furthermore, it was revealed by theoretical calculations that the CMC possesses much higher binding energy towards Na-ion than PVDF. As shown in Fig. 5h, CMC has two binding sites with $Na^+$, and the $\Delta E1$ and $\Delta E2$ are 3.85 eV and 3.31 eV, respectively, whereas PVDF has only one binding site with $\Delta E$ is 1.04. Thus, the electrode with CMC binder possesses a stronger chelating ability to capture sodium, which substantiates Na-ion desolvation and enhances the reaction kinetics.

The composition of the PNC electrode after 5 cycles in different
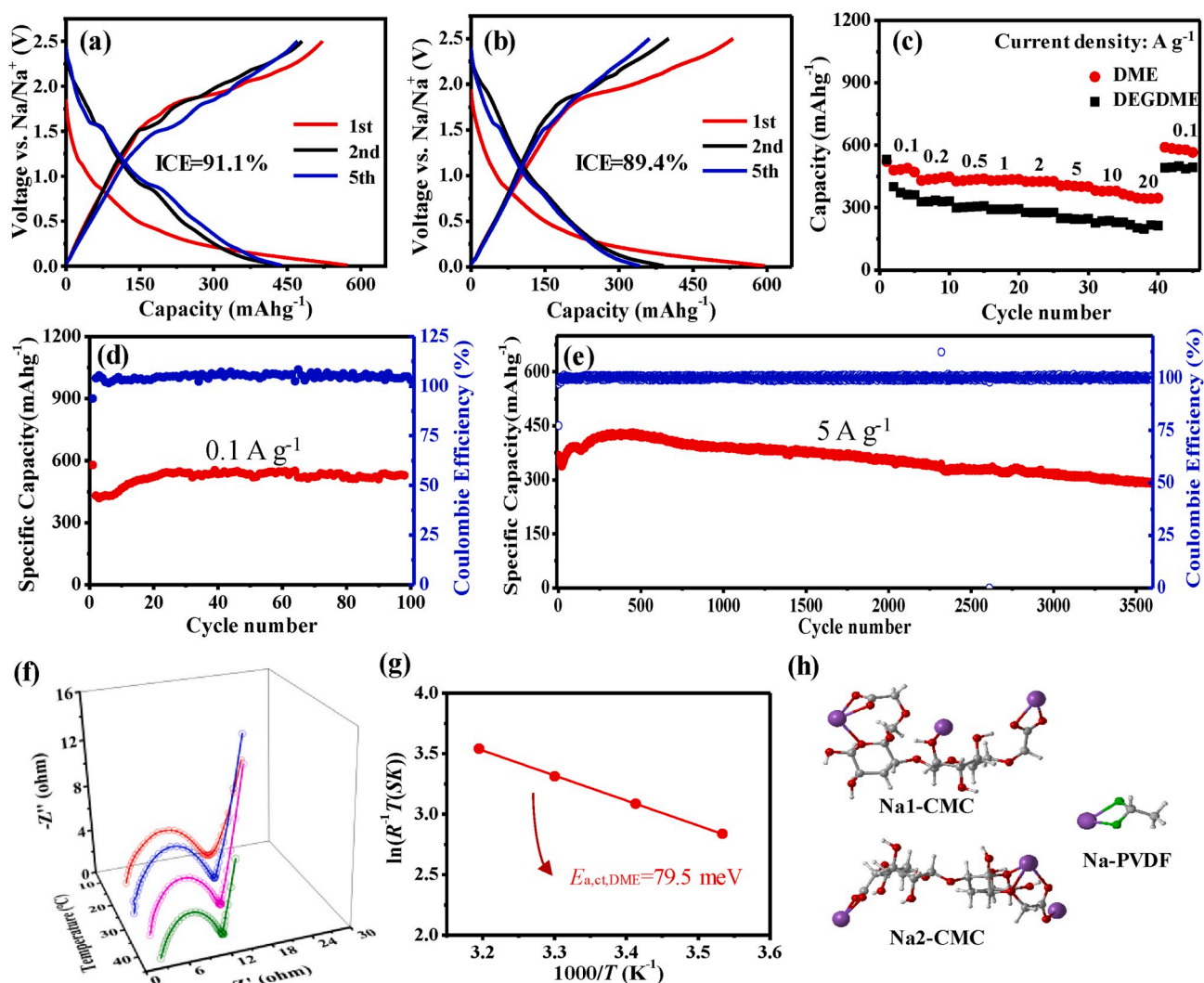
**Fig. 5.** Discharge and charge profiles for the 1st, 2nd and 5th cycles of PNC anode (CMC binder) in (a) DME and (b) DEGDME electrolytes at a rate of 0.1 A $g^{-1}$. (c) Rate capability of PNC in different electrolytes. (d) Cycling performance in DME electrolyte of 100 cycles at 0.1 A $g^{-1}$ and (e) long-term life evaluation for 3600 cycles at 5 A $g^{-1}$. (f)Temperature-dependent Nyquist plots of the PNC anode (CMC binder) in DME-based electrolyte. (g) Corresponding Arrhenius plot of activation energies $E_{a,ct}$ for PNC anode. (h) The binding configurations of $Na^+$ with two kinds of binders.

electrolytes were studied, as shown in Fig. 6a, Fig. 6b and Table S5. Both electrodes displayed a homogeneous distribution of C, O, Na, P and F elements while the EDX results confirmed the lower contents of Na and O elements for PNC in ether electrolyte, indicating less decomposition of electrolytes on the electrode surfaces and reduced amount of irreversible sodiation processes [51]. The surface state of each SEI layer were further explored by XPS (Fig. S11). Fig. 6c–e show the C1s, O1s and F1s XPS spectra for cycled PNC electrodes. The peaks at 284.8, 285.8, 286.6, 288.2 and 289.4 eV in C1s spectrum are consistent with C–C, C–H, C–O, C=O and RCH$_2$ONa, respectively. The O1s spectrum with a peak at ~531.6 eV is ascribed to C=O, which could come from sodium alkyl carbonate or sodium carboxylate. The broad peaks at 533.1 eV revealed the presence of C–O and 532.1 eV may come from RSO$_3$Na [51]. The F1s spectra in EC/DMC electrolyte displayed additional peaks at 684.7 and 687.4 eV, which clearly identified the presence of NaF and Na$_2$PO$_3$F [64, 65], respectively. The XRD patterns (Fig. S12) also found them, indicating the relative serious decomposition of NaPF$_6$ in ester electrolytes [66]. The SEM images of PNC electrode in DME and EC/DMC electrolytes after five cycles are shown in Fig. S13. The nanosheets morphology can be observed and a thin SEI is formed in DME electrolytes. While in EC/DEC electrolyte, the electrode is covered by a thick SEI layer due to serious decomposition, as further revealed by EDX mapping (Fig. 6b).

Fig. 6f depicts the schematic mechanism of sodium-ion desolvation and transport process in the different electrolytes. Due to intense adsorption of solvated Na-ion on graphene planes in ester electrolyte, the electrolyte including solvent and the accompanying PF$_6^-$ would decompose, resulting in a thick SEI layer on the surface of PNC electrode and a large $E_{a,SEI}$. However, this can be remarkably inhibited in ether electrolytes owing to the fast Na-ion desolvation and transport process at the electrode surface, leading to a thin SEI layer, few irreversible capacities lost and exceptional kinetics.

## 3. Conclusion

It is proposed and demonstrated that $Na^+$ desolvation barrier at electrolyte/electrode interface poses a predominant effect on the sodium ion storage capacity of the electrode material. Through comprehensive study of different carbon anodes in ester and ether electrolyte, it was shown that nanocarbon electrode with small interlayer spacing but very high surface area displayed few side reactions at the interface, exceptional kinetics and excellent cycling stability in ether electrolytes. This can be due to the remarkably reduced $Na^+$ desolvation barrier in ether electrolytes, which is only one-third of that found in ester electrolytes. The DFT calculations verified that Na-ion desolvation process in ether-
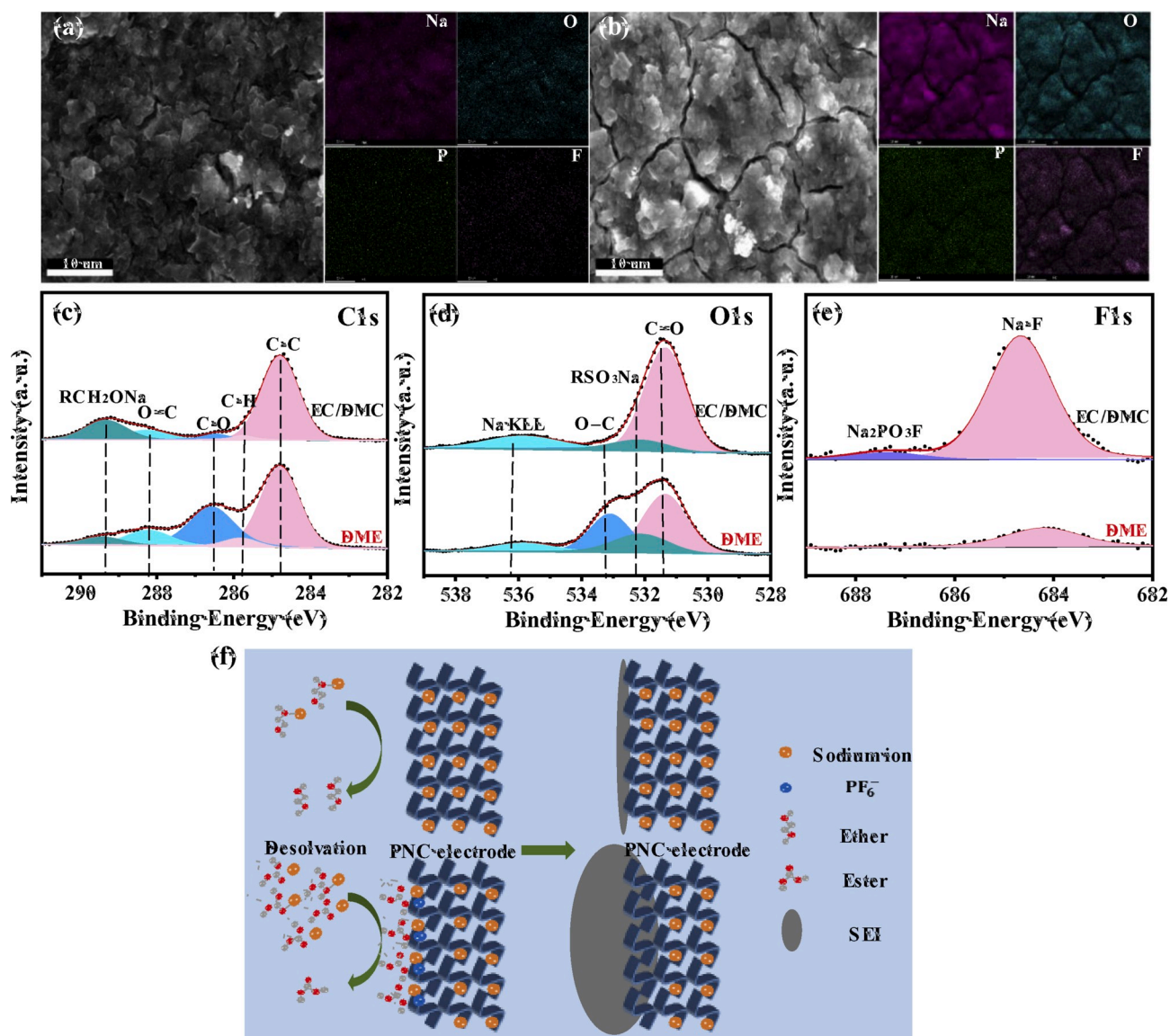
**Fig. 6.** The elements mapping of PNC anode with CMC binder in DME (a) and EC/DMC (b) electrolytes after the five cycles. Surface composition characterization of SEI layers by XPS: (c) C 1s, (d) O 1s, and (e) F 1s spectra for PNC electrodes in DME and EC/DMC electrolytes after five cycles. (f) Schematic mechanism of sodium-ion transport and desolvation process in different electrolytes.

based electrolytes is energetically favored when compared to the ester-based electrolytes. Moreover, the too strong Na-ion adsorption on graphene planes in ester solvents can also be overcome in ether solvents due to the lower values of Gibbs free energies for Na adsorption. This study demonstrates how Na-ion transport kinetics at the electrode surface play a key role on the performance, providing a reliable model for the understanding and design of compatible electrolytes with electrode materials in rechargeable batteries.

## Declaration of competing interest

The authors declare no competing financial interest.

## CRediT authorship contribution statement

**Yichao Zhen:** Formal analysis, Writing - original draft. **Rongjian Sa:** Formal analysis, Writing - original draft. **Kaiqiang Zhou:** Formal analysis. **Lingyi Ding:** Formal analysis. **Yang Chen:** Formal analysis. **Sanjay Mathur:** Supervision, Formal analysis. **Zhensheng Hong:** Supervision, Formal analysis.

## Appendix A. Supplementary data

Supplementary data to this article can be found online at https://doi.org/10.1016/j.nanoen.2020.104895.

## References

[1] H. Kang, Y. Liu, K. Cao, Y. Zhao, L. Jiao, Y. Wang, H. Yuan, J. Mater. Chem. 3 (2015) 17899–17913.
[2] H. Kim, H. Kim, Z. Ding, M.H. Lee, K. Lim, G. Yoon, K. Kang, Adv. Energy Mater. 6 (2016) 1600943–1600981.

[3] S.-W. Kim, D.-H. Seo, X. Ma, G. Ceder, K. Kang, Adv. Energy Mater. 2 (2012) 710–721.
[4] V. Palomares, P. Serras, I. Villaluenga, K.B. Hueso, J. Carretero-González, T. Rojo, Energy Environ. Sci. 5 (2012) 5884–5901.
[5] N. Yabuuchi, K. Kubota, M. Dahbi, S. Komaba, Chem. Rev. 114 (2014) 11636–11682.
[6] W. Luo, F. Shen, C. Bommier, H. Zhu, X. Ji, L. Hu, Acc. Chem. Res. 49 (2016) 231–240.
[7] J.Y. Hwang, S.T. Myung, Y.K. Sun, Chem. Soc. Rev. 46 (2017) 3529–3614.
[8] M.Á. Muñoz-Márquez, D. Saurel, J.L. Gómez-Cámer, M. Casas-Cabanas, E. Castillo-Martínez, T. Rojo, Adv. Energy Mater. 7 (2017) 1700463–1700494.
[9] T. Liu, Y. Zhang, Z. Jiang, X. Zeng, J. Ji, Z. Li, X. Gao, M. Sun, Z. Lin, M. Ling, J. Zheng, C. Liang, Energy Environ. Sci. 12 (2019) 1512–1533.
[10] Z. Hong, Y. Zhen, Y. Ruan, M. Kang, K. Zhou, J.M. Zhang, Z. Huang, M. Wei, Adv. Mater. 30 (2018) 1802035–1802044.
[11] J. Han, G. Huang, Z. Wang, Z. Lu, J. Du, H. Kashani, M. Chen, Adv. Mater. 30 (2018) 1803588–1803596.
[12] F. Xie, Z. Xu, A.C.S. Jensen, H. Au, Y. Lu, V. Araullo-Peters, A.J. Drew, Y.S. Hu, M. M. Titirici, Adv. Funct. Mater. 29 (2019) 1901072–1901081.
[13] M. Liu, P. Zhang, Z. Qu, Y. Yan, C. Lai, T. Liu, S. Zhang, Nat. Commun. 10 (2019) 3917–3928.
[14] Y. Cao, L. Xiao, M.L. Sushko, W. Wang, B. Schwenzer, J. Xiao, Z. Nie, L.V. Saraf, Z. Yang, J. Liu, Nano Lett. 12 (2012) 3783–3787.
[15] K. Tang, L. Fu, R.J. White, L. Yu, M.-M. Titirici, M. Antonietti, J. Maier, Adv. Energy Mater. 2 (2012) 873–877.
[16] X. Xiong, C. Yang, G. Wang, Y. Lin, X. Ou, J.-H. Wang, B. Zhao, M. Liu, Z. Lin, K. Huang, Energy Environ. Sci. 10 (2017) 1757–1763.
[17] M. Lao, Y. Zhang, W. Luo, Q. Yan, W. Sun, S.X. Dou, Adv. Mater. 29 (2017) 1700622–1700645.
[18] W. Li, S.L. Chou, J.Z. Wang, J.H. Kim, H.K. Liu, S.X. Dou, Adv. Mater. 26 (2014) 4037–4042.
[19] N. Zhang, X. Han, Y. Liu, X. Hu, Q. Zhao, J. Chen, Adv. Energy Mater. 5 (2015) 1401123–1401130.
[20] X. Xia, D. Chao, Y. Zhang, J. Zhan, Y. Zhong, X. Wang, Y. Wang, Z.X. Shen, J. Tu, H. J. Fan, Small 12 (2016) 3048–3058.
[21] P. He, Y. Fang, X.Y. Yu, X.W.D. Lou, Angew. Chem. Int. Ed. 56 (2017) 12202–12205.
[22] Y. Xiao, S.H. Lee, Y.-K. Sun, Adv. Energy Mater. 7 (2017) 1601329–1601349.
[23] M.N. Tahir, B. Oschmann, D. Buchholz, X. Dou, I. Lieberwirth, M. Panthofer, W. Tremel, R. Zentel, S. Passerini, Adv. Energy Mater. 6 (2016) 1501489–1501498.
[24] M. Kang, Y. Ruan, Y. Lu, L. Luo, J. Huang, J.-M. Zhang, Z. Hong, J. Mater. Chem. 7 (2019) 16937–16946.
[25] Z. Hong, M. Kang, X. Chen, K. Zhou, Z. Huang, M. Wei, ACS Appl. Mater. Interfaces 9 (2017) 32071–32079.
[26] J. Yang, X. Xiao, W. Gong, L. Zhao, G. Li, K. Jiang, R. Ma, M.H. Rummeli, F. Li, T. Sasaki, F. Geng, Angew. Chem. Int. Ed. 58 (2019) 8740–8745.
[27] Z. Li, C. Bommier, Z.S. Chong, Z. Jian, T.W. Surta, X. Wang, Z. Xing, J. C. Neuefeind, W.F. Stickle, M. Dolgos, P.A. Greaney, X. Ji, Adv. Energy Mater. 7 (2017) 1602894–1602904.
[28] P. Bai, Y. He, X. Zou, X. Zhao, P. Xiong, Y. Xu, Adv. Energy Mater. 8 (2018) 1703217–1703226.
[29] S. Alvin, D. Yoon, C. Chandra, H.S. Cahyadi, J.-H. Park, W. Chang, K.Y. Chung, J. Kim, Carbon 145 (2019) 67–81.
[30] X. Dou, I. Hasa, D. Saurel, C. Vaalma, L. Wu, D. Buchholz, D. Bresser, S. Komaba, S. Passerini, Mater. Today 23 (2019) 87–104.
[31] S. Komaba, W. Murata, T. Ishikawa, N. Yabuuchi, T. Ozeki, T. Nakayama, A. Ogata, K. Gotoh, K. Fujiwara, Adv. Funct. Mater. 21 (2011) 3859–3867.
[32] S. Huang, Z. Li, B. Wang, J. Zhang, Z. Peng, R. Qi, J. Wang, Y. Zhao, Adv. Funct. Mater. 28 (2018) 1706294–1706304.
[33] G. Yoon, H. Kim, I. Park, K. Kang, Adv. Energy Mater. 7 (2017) 1601519–1601528.
[34] H. Kim, J. Hong, Y.-U. Park, J. Kim, I. Hwang, K. Kang, Adv. Funct. Mater. 25 (2015) 534–541.
[35] B. Adv, Jache. P. Adelhelm, Energy Mater. Angew. Chem. Int. Ed. 53 (2014) 10169–10173.
[36] Z.L. Xu, G. Yoon, K.Y. Park, H. Park, O. Tamwattana, S. Joo Kim, W.M. Seong, K. Kang, Nat. Commun. 10 (2019) 2598–2608.
[37] G. Zou, C. Wang, H. Hou, C. Wang, X. Qiu, X. Ji, Small 13 (2017) 1700762–1700772.
[38] J. Yang, X. Zhou, D. Wu, X. Zhao, Z. Zhou, Adv. Mater. 29 (2017) 1604108–1604113.
[39] L. Qie, W. Chen, X. Xiong, C. Hu, F. Zou, P. Hu, Y. Huang, Adv. Sci. 2 (2015) 1500195–1500201.
[40] Y. Yang, D.-M. Tang, C. Zhang, Y. Zhang, Q. Liang, S. Chen, Q. Weng, M. Zhou, Y. Xue, J. Liu, J. Wu, Q.H. Cui, C. Lian, G. Hou, F. Yuan, Y. Bando, D. Golberg, X. Wang, Energy Environ. Sci. 10 (2017) 979–986.
[41] C. Bommier, T.W. Surta, M. Dolgos, X. Ji, Nano Lett. 15 (2015) 5888–5892.
[42] S. Qiu, L. Xiao, M.L. Sushko, K.S. Han, Y. Shao, M. Yan, X. Liang, L. Mai, J. Feng, Y. Cao, X. Ai, H. Yang, J. Liu, Adv. Energy Mater. 7 (2017) 1700403–1700414.
[43] D. Datta, J. Li, V.B. Shenoy, ACS Appl. Mater. Interfaces 6 (2014) 1788–1795.
[44] P.-c. Tsai, S.-C. Chung, S.-k. Lin, A. Yamada, J. Mater. Chem. 3 (2015) 9763–9768.
[45] Y. Liu, B.V. Merinov, W.A. Goddard 3rd, Proc. Natl. Acad. Sci. Unit. States Am. 113 (2016) 3735–3739.
[46] Y. Li, L. Mu, Y.-S. Hu, H. Li, L. Chen, X. Huang, Energy Storage Mater 2 (2016) 139–145.
[47] W. Luo, C. Bommier, Z. Jian, X. Li, R. Carter, S. Vail, Y. Lu, J.J. Lee, X. Ji, ACS Appl. Mater. Interfaces 7 (2015) 2626–2631.
[48] J. Xu, M. Wang, N.P. Wickramaratne, M. Jaroniec, S. Dou, L. Dai, Adv. Mater. 27 (2015) 2042–2048.
[49] Y. Yan, Y.-X. Yin, Y.-G. Guo, L.-J. Wan, Adv. Energy Mater. 4 (2014) 1301584–1301589.
[50] Y.-X. Wang, S.-L. Chou, H.-K. Liu, S.-X. Dou, Carbon 57 (2013) 202–208.
[51] J. Zhang, D.-W. Wang, W. Lv, S. Zhang, Q. Liang, D. Zheng, F. Kang, Q.-H. Yang, Energy Environ. Sci. 10 (2017) 370–376.
[52] M. Kang, Y. Wu, X. Huang, K. Zhou, Z. Huang, Z. Hong, J. Mater. Chem. 6 (2018) 22840–22850.
[53] K. Li, J. Zhang, D. Lin, D.W. Wang, B. Li, W. Lv, S. Sun, Y.B. He, F. Kang, Q.H. Yang, L. Zhou, T.Y. Zhang, Nat. Commun. 10 (2019) 725–735.
[54] J. Huang, X. Guo, X. Du, X. Lin, J.-Q. Huang, H. Tan, Y. Zhu, B. Zhang, Energy Environ. Sci. 12 (2019) 1550–1557.
[55] B.H. Hou, Y.Y. Wang, Q.L. Ning, W.H. Li, X.T. Xi, X. Yang, H.J. Liang, X. Feng, X. L. Wu, Adv. Mater. 31 (2019), e1903125.
[56] V. Augustyn, J. Come, M.A. Lowe, J.W. Kim, P.L. Taberna, S.H. Tolbert, H. D. Abruna, P. Simon, B. Dunn, Nat. Mater. 12 (2013) 518–522.
[57] K. Zhao, F. Liu, C. Niu, W. Xu, Y. Dong, L. Zhang, S. Xie, M. Yan, Q. Wei, D. Zhao, L. Mai, Adv. Sci. 2 (2015), 1500154.
[58] Y. Yamada, Y. Iriyama, T. Abe, Z. Ogumi, Langmuir 25 (2009) 12766–13770.
[59] K. Xu, A. von Cresce, U. Lee, Langmuir 26 (2010) 11538–11543.
[60] M.R. Busche, T. Drossel, T. Leichtweiss, D.A. Weber, M. Falk, M. Schneider, M. L. Reich, H. Sommer, P. Adelhelm, J. Janek, Nat. Chem. 8 (2016) 426–434.
[61] Z.-L. Xu, K. Lim, K.-Y. Park, G. Yoon, W.M. Seong, K. Kang, Adv. Funct. Mater. 28 (2018) 1802099–1802109.
[62] S. Komaba, T. Ozeki, K. Okushi, J. Power Sources 189 (2009) 197–203.
[63] K. Zhou, M. Kang, X. He, Z. Hong, Z. Huang, M. Wei, J. Mater. Chem. 5 (2017) 18138–18147.
[64] L. Bodenes, A. Darwiche, L. Monconduit, H. Martinez, J. Power Sources 273 (2015) 14–24.
[65] Y. Pan, Y. Zhang, B.S. Parimalam, C.C. Nguyen, G. Wang, B.L. Lucht, J. Electroanal. Chem. 799 (2017) 181–186.
[66] G.G. Eshetu, T. Diemant, M. Hekmatfar, S. Grugeon, R.J. Behm, S. Laruelle, M. Armand, S. Passerini, Nano Energy 55 (2019) 327–340.

**Yichao Zhen** received his B.S. degree in June 2018 from Fujian Normal University, China. He is now pursuing the M.S. degree under the supervision of Prof. Zhensheng Hong in the College of Physics and Energy at Fujian Normal University, Fuzhou, Fujian 350117, China. He research is focused on the fabrication of nanomaterials for Na/K-ion batteries.

**Rongjian Sa** is an associate professor at Institute of Oceanography, Minjiang University, China. He received his PhD degree in June 2005 from Shanghai Institute of Materia Medica, Chinese Academy of Sciences. He then worked as an associate professor at Fujian Institute of Research on the Structure of Mater, Chinese Academy of Sciences from 2005 to 2018. His current research interests focus on the application of computational chemistry in energy material and catalysis design.

**Kaiqiang Zhou** received her B.S. degree in June 2014 from Fujian Normal University, China. Beginning in September 2014, he is continuously undertaking the M. S. and Ph.D. degree under the guidance of Prof. Hong Zhensheng at College of Physics and Energy, Fujian Normal University, Fuzhou, Fujian, China. His research is focused on the fabrication of nanomaterials for alkali-ion batteries.
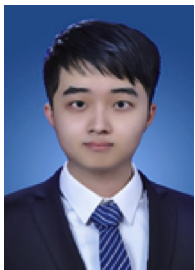
**Lingyi Ding** is currently studying at Fujian Normal University, China. With the guidance of Prof. Hong Zhensheng at College of Physics and Energy, she is studying for an undergraduate degree. Her research focus is on the manufacture of new two-dimensional materials.

**Prof. Sanjay Mathur** is Director and Chair of the Institute of Inorganic Chemistry at University of Cologne, Germany. He is an Academician of the World Academy of Ceramics. A Fellow of the American Ceramics Society and ASM International. Mathur earned a DPhil in Chemical Laboratories from University of Rajasthan, and M.Phil. and M.Sc. in Physical Chemistry from Vikram University in India. His research interests focus on application of nanomaterials and advanced ceramics for energy technologies. He is an Academician of the World Academy of Ceramics.

**Yang Chen** received his B.S. degree in June 2019 from Fujian Normal University, China. He is currently a M.S. student under the guidance of Prof. Hong Zhensheng at College of Physics and Energy, Fujian Normal University, Fuzhou, Fujian, China. His research focuses on the fabrication of nanomaterials for Li-ion batteries.

**Zhensheng Hong** is a Professor of College of Physics and Energy at Fujian Normal University, Fuzhou, China. He received his B.S. and Ph.D. degree from Fuzhou University, China. He received a Humboldt Research Fellowship for Experienced Researchers in 2018 and conducted the joint study with Prof. Sanjay Mathur in the University of Cologne, Germany. His research interests include rational design of electrode materials for energy storage and conversion, electrochemistry at surface/interface. He has authored and co-authored over 65 papers and granted 20 patents.